Autoinhibition of ubiquitin-specific protease 8: Insights into domain interactions and mechanisms of regulation

Cody Caba[1] , Megan Black[2], Yujue Liu[3], Ashley A. DaDalt[1,4], Josh Mallare[1], Lixin Fan[5], Rachel J. Harding[6,7],
Yun-Xing Wang[8], Panayiotis O. Vacratsis[1], Rui Huang[2], Zhihao Zhuang[3], and Yufeng Tong[1,*]

From the [1]Department of Chemistry and Biochemistry, University of Windsor, Windsor, Canada; [2]Department of Chemistry,
University of Guelph, Guelph, Canada; [3]Department of Chemistry and Biochemistry, University of Delaware, Newark, Delaware,
USA; [4]Department of Biology, University of Michigan-Dearborn, Dearborn, Michigan, USA; [5]Basic Science Program, Frederick
National Laboratory for Cancer Research, Small-Angle X-ray Scattering Core Facility, National Cancer Institute, National Institutes
of Health, Frederick, Maryland, USA; [6]Structural Genomics Consortium, and [7]Department of Pharmacology and Toxicology,
University of Toronto, Toronto, Canada; [8]Center for Structural Biology, National Cancer Institute at Frederick, National Institutes
of Health, Frederick, Maryland, USA

Reviewed by members of the JBC Editorial Board. Edited by George DeMartino

Ubiquitin-specific proteases (USPs) are a family of multi-domain deubiquitinases (DUBs) with variable architectures, some containing regulatory auxiliary domains. Among the USP family, all occurrences of intramolecular regulation presently known are autoactivating. USP8 remains the sole exception as its putative WW-like domain, conserved only in vertebrate orthologs, is autoinhibitory. Here, we present a comprehensive structure–function analysis describing the autoinhibition of USP8 and provide evidence of the physical interaction between the WW-like and catalytic domains. The solution structure of full-length USP8 reveals an extended, monomeric conformation. Coupled with DUB assays, the WW-like domain is confirmed to be the minimal autoinhibitory unit. Strikingly, autoinhibition is only observed with the WW-like domain in *cis* and depends on the length of the linker tethering it to the catalytic domain. Modeling of the WW:CD complex structure and mutagenesis of interface residues suggests a novel binding site in the S1 pocket. To investigate the interplay between phosphorylation and USP8 autoinhibition, we identify AMP-activated protein kinase as a highly selective modifier of S718 in the 14-3-3 binding motif. We show that 14-3-3γ binding to phosphorylated USP8 potentiates autoinhibition in a WW-like domain-dependent manner by stabilizing an autoinhibited conformation. These findings provide mechanistic details on the autoregulation of USP8 and shed light on its evolutionary significance.

Ubiquitination plays a crucial role in molecular quality control and is necessary for many protein-protein interactions (PPIs). In humans, there are over 1000 writers of the Ub code, while only about 100 erasers exist, known as the deubiquitinases (DUBs). Fifty-seven of these DUBs belong to the USP subfamily (1, 2). USPs are generally the largest, and most have a multidomain architecture (3). Among the 51 catalytically active USPs, the activity and regulation of relatively few have been thoroughly studied. Nonetheless, there are multiple examples of regulation by intramolecular mechanisms mediated by auxiliary domains (4). For instance, in USP7, the C-terminal HAUSP Ub-like (HUBL) domain binds to a switching loop in the catalytic domain (CD), leading to a 100-fold increase in its activity (5). In USP4, the tandem N-terminal DUSP (domain in USP) and Ubl domains augment catalytic turnover by promoting substrate release (6). Currently, the only examples of autoinhibition are observed in USP25, which is autoinhibited intermolecularly by tetramerization (7, 8), and USP8, which is autoinhibited intramolecularly by a putative WW-like domain (9). While the autoinhibitory mechanism of USP25 is well-established, that governing USP8 is not.

USP8 is a 130 kDa DUB comprised of three well-characterized, structure-resolved domains (10, 11): an N-terminal microtubule interacting and transport (MIT) domain that binds charged multivesicular body proteins (CHMPs) of the early and late endosomes (12), an adjacent rhodanese-like (Rhod) domain that interacts with the E3 ligase NRDP1 (10, 13), and a C-terminal CD. A predicted intrinsically disordered region (IDR) 460 a.a. long connects the N-terminal MIT-Rhod to the CD (Fig. 1A). This linker contains three atypical RXXK SH3 binding motifs (SH3BM) that interact with endosomal ESCRT-0 proteins STAM1/2 (14), and a conserved 14-3-3 binding motif (14-3-3BM) containing a phosphorylated serine (S718 in humans) for which the kinase responsible is unknown.

USP8 is an important therapeutic target because of its essentiality in many cancers (15). Most famously, somatic mutations in the 14-3-3BM drive a subset of pituitary adenomas, causing the rare endocrine disorder Cushing's disease (16, 17). When such mutations disrupt the binding to 14-3-3 proteins, USP8 is cleaved at K714 to yield a 40 kDa hyperactive catalytic fragment (17). In pituitary adenoma, this hyperactive proteoform increases the recycling of EGF receptors to the plasma membrane, where sustained signaling causes an abnormal
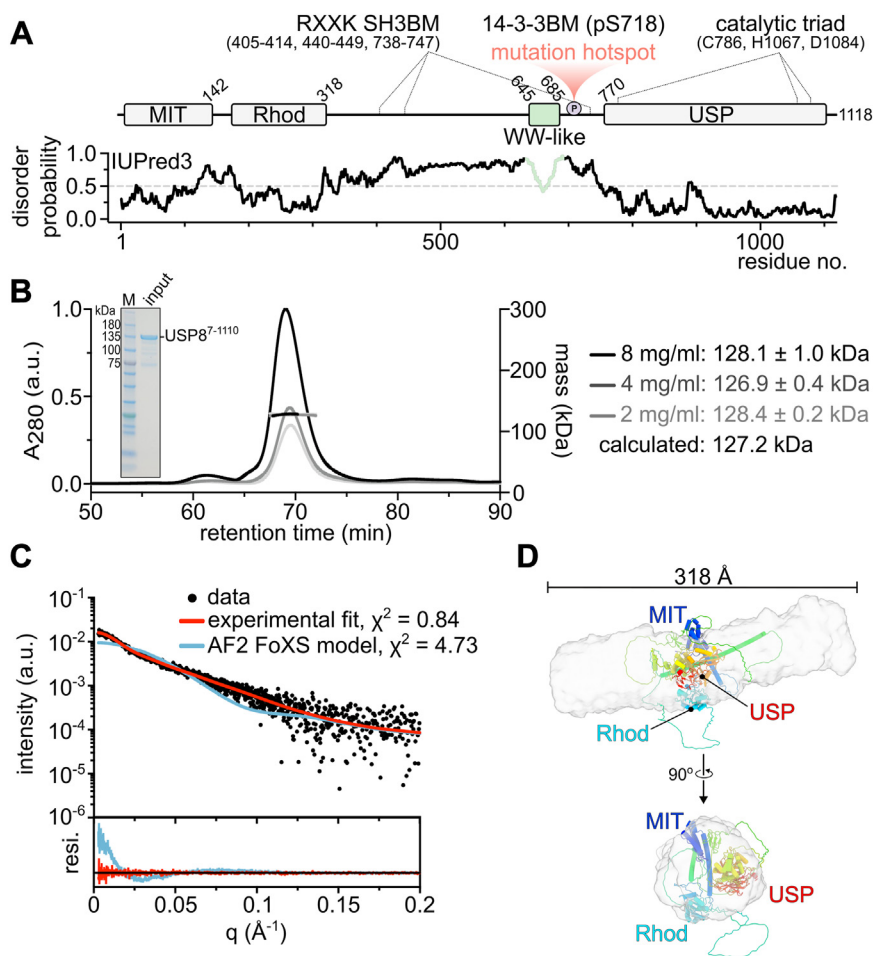
Figure 1. Solution structure of USP8. *A*, schematic representation of human USP8 aligned with the predicted disorder probability plot. The WW-like autoinhibitory domain is in *green*. 14-3-3BM, 14-3-3 binding motif; MIT, microtubule interacting and transport; Rhod, rhodanese-like; USP, Ub-specific protease domain. *B*, SEC-MALLS of FL USP8 at the indicated concentrations. *C*, SEC-SAXS data was collected from FL USP8 (*black dots*), and the corresponding fit and residuals were calculated using GNOM (*red*). The theoretical scattering profile from the AF2 model (af-p40818-f1) was calculated using FoXS (blue). *D*, *Ab initio* envelope generated from the experimental data and superimposed with the AF2 model of USP8.

increase of adrenocorticotropic hormone synthesis and secretion (17). The observation that FL USP8 is significantly less active than the CD fragment puts into question the molecular basis of this discrepancy. Recently, a putative WW-like domain upstream and adjacent to the CD was shown to autoinhibit USP8 (9). Kakihara and coauthors relied on computational methods, disruptive FRET constructs, and crude enzyme preparations to resolve this, leaving mechanistic details unclear. Whereas canonical WW domains contain two signature tryptophan residues, the USP8 WW-like domain has only one. However, we henceforth refer to it as a WW domain for simplicity.

In this study, we have determined the mechanism of USP8 autoinhibition by the WW domain. Using biophysical and biochemical techniques, we demonstrate that USP8 is monomeric and extended in solution and that a folded WW domain is the minimal autoinhibitory unit. Interestingly, USP8 activity was only inhibited by the WW domain in *cis*, likely mediated by a proximity-dependent interaction with the CD. Modeling using AlphaFold-Multimer resolved a novel WW:CD complex structure with the WW domain occupying the S1 Ub binding

pocket. We also examined the binding of 14-3-3γ to phosphorylated USP8 and found it potentiated autoinhibition, whereas 14-3-3γ binding to a WW domain-deleted mutant had no effect. Sequence alignments indicate the WW domain, and 14-3-3BM may be co-evolved features exclusive to vertebrate orthologs, suggesting an evolutionarily acquired regulatory mechanism for low basal activity.

Results

Full-length USP8 is an extended monomer in solution

To understand the allosteric regulation of USP8, we first sought to resolve the structure of the FL human enzyme. Extensive optimization resulted in a purifiable construct encompassing a.a. 7 to 1110. To our knowledge, this is the first purification protocol described for FL USP8 that yields protein suitable for biophysical assays (Fig. S1). Size exclusion chromatography-coupled multi-angle laser light scattering (SEC-MALLS) revealed a molecular weight of ∼128 kDa, in agreement with the calculated monomer mass of 127 kDa (Fig. 1*B*). This is in contrast to previous reports of dimerization

about the N-terminal MIT domain (9, 10); thus our data suggest this may be a crystal packing artifact.

Due to its large size and the central intrinsically disordered region, USP8 is refractory to high-resolution structure determination methods. Small-angle X-ray scattering (SAXS) was used to ascertain the average conformational ensemble in solution (18) (Table S1). As expected for flexible proteins with significant stretches of disorder, the estimated radius of gyration (R_g) for USP8 was relatively variable and ranged from 70 to 87 Å (Fig. S2A). We performed singular value decomposition (SVD) on nine frames (1162–1170) central to the elution profile and determined the existence of one molecular component therein (Fig. S2B). The scattering profile obtained from the selected frames was smooth and featureless (Fig. 1C), and the Guinier plot was linear (Fig. S2C)—several lines of evidence point to a flexible, extended conformation for USP8 (19). First, the dimensionless Kratky plot was open-ended, with a maximum shift to higher values relative to the coordinates expected for a globular particle ((1.73, 1.10)) (Fig. S2D). Second, the pairwise distance distribution function ($P(r)$) had a shape consistent with an extended rod-shaped particle and a large 318 Å D_{max} (Fig. S2E). Lastly, recent proteome-scale ensemble modeling of the two primary IDRs in USP8, the MIT-Rhod linker spanning a.a. 130 to 187 and the central IDR spanning a.a. 315 to 756, showed that the former is significantly expanded (Flory scaling exponent (ν) = 0.571). The latter is an 'ideal chain' with an average degree of expansion (ν = 0.527) (20). This indicates that the extended conformation of USP8 resolved by SAXS can partly be explained by the length and composition of its IDRs.

Next, we compared the AlphaFold2 (AF2) model of USP8 (af-p40818-f1) to our *ab initio* envelope derived from scattering data. The compact AF2 model has high predicted aligned error (PAE) for interdomain residue pairs (PAE ≈30 Å), suggesting low confidence in relative domain arrangements (Fig. S3). A computed scattering curve of this model using FoXS (21) rendered a much smaller estimated R_g of 45.9 Å and was a poor fit to the experimental profile (Fig. 1C). Thus, the SAXS data presented here show that USP8 is an extended, rod-shaped protein in solution (Fig. 1D).

The WW domain is an inhibitory module tethered to the catalytic domain

In USP8-mutant Cushing's disease, a dysregulated hyperactive catalytic fragment is proposed to underlie the pathology (17). We therefore examined the autoinhibition of USP8 by measuring the DUB activity of various constructs (Fig. 2A) using the fluorogenic 7-amido-4-methylcoumarin-derived Ub (Ub-AMC) minimal substrate (Fig. S4 and Table S2). As expected, deletion of the entire N-terminus (a.a. 1–733), which
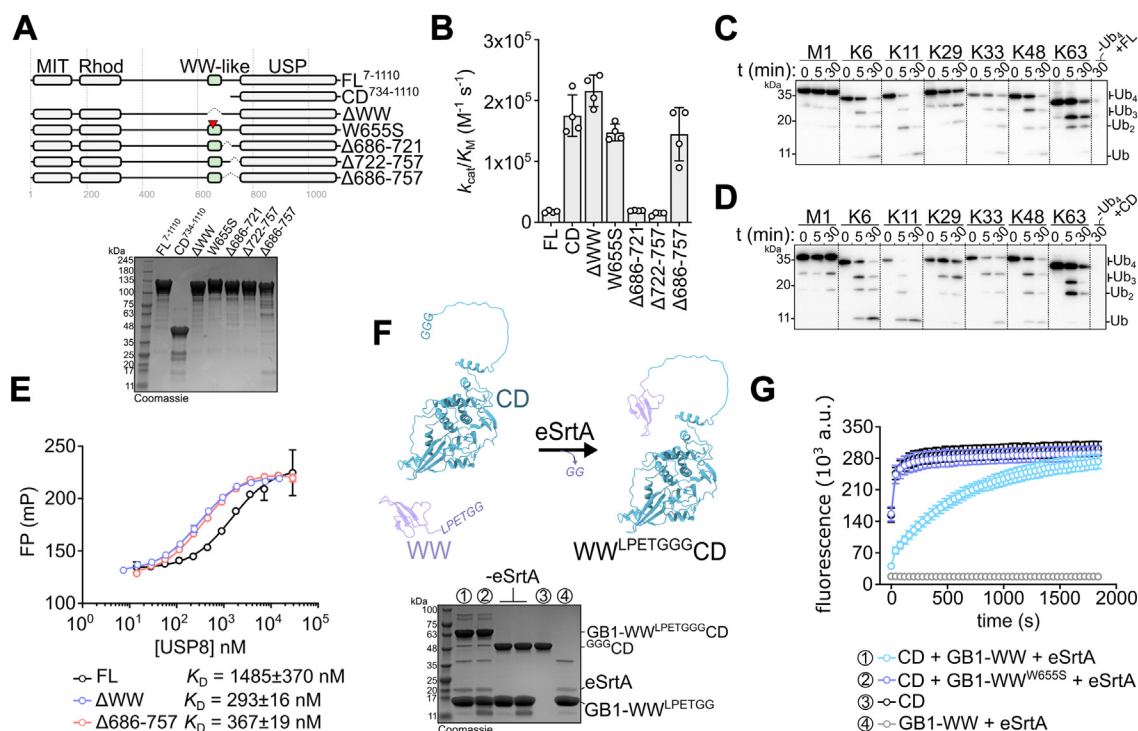
Figure 2. The WW domain inhibits USP8 in *cis*. *A*, Domain architecture and final purification products of the USP8 constructs used in this study. *B*, catalytic efficiency of USP8 constructs measured using the Ub-AMC substrate (n = 4). *C* and *D*, Tetra-Ub cleavage assays using 200 nM USP8 FL (*C*) and 40 nM CD (*D*). Ub$_4$ at a concentration of 0.5 μM was incubated with USP8, and samples were taken after 0, 5, and 30 min. Products of the reaction were analyzed by immunoblot using an anti-Ub antibody. *E*, equilibrium binding of USP8 FL, USP8$^{\Delta WW}$, and USP8$^{\Delta 686–757}$ to mono-Ub. Binding was assessed by fluorescence polarization using 2 nM mono-Ub with an N-terminal fluorescein moiety. Data represent the mean and standard deviation of two independent experiments. *F*, depiction of sortase-mediated ligation (SML) of WW^{LPETGG} and ^{GGG}CD$^{691–1110}$ generating the WW^{LPETGGG}CD product. The reaction was performed using 200 μM GB1-WW^{LPETGG} or GB1-WW$^{W655S.LPETGG}$, 20 μM ^{GGG}CD$^{691–1110}$, and 5 μM eSrtA. (*G*) SML samples 1 to 4 from *F* were diluted 800-fold and assayed for DUB activity using 2 μM Ub-AMC (n = 3).

contains the putative WW domain (a.a. 645–685) previously described as an autoinhibitory module (9), resulted in a hyperactive CD with catalytic efficiency (k_{cat}/K_M) ten-fold greater ((176 ± 20) $\times 10^3$ M^{-1} s^{-1}) than FL ((17 ± 1) $\times 10^3$ M^{-1} s^{-1}) (Fig. 2*B*). We compared the ability of FL and CD constructs to deconjugate native, homotypic tetra-Ub (Ub$_4$) to determine if a difference in the poly-Ub linkage preference was present. While it took five times more FL (Fig. 2*C*) to qualitatively match the activity of CD (Fig. 2*D*), both constructs had similarly promiscuous proteolytic profiles. Except for linear Ub$_4$ (M1-linked), all linkages (K6, K11, K29, K33, K48, and K63; K27 not tested) were cleaved. In support of a recent report (22), we noted that USP8 was most active towards K11-linked poly-Ub and least active towards K29-linked under our conditions. We also noted linkage-dependent differential mobility of poly-Ub on SDS-PAGE, especially for Ub$_4$ and Ub$_3$ polymers. This is a common occurrence and has been highlighted previously (23). Overall, these data indicate the N-terminus attenuates DUB activity but does not influence the poly-Ub linkage preference of USP8.

We next confirmed the WW domain as the minimal autoinhibitory unit by measuring the DUB activity of a WW domain-deleted mutant (USP8$^{\Delta WW}$), which revealed similar activity as CD and a twelve-fold greater catalytic efficiency ((215 ± 49) $\times 10^3$ M^{-1} s^{-1}) compared to FL (Fig. 2*B*). Likewise, WW-mediated autoinhibition of USP8 DUB activity was also observed in the mouse ortholog (Fig. S5).

The invariant N-terminal tryptophan of WW domains is structurally important (24, 25). This residue in USP8 is W655, which is on the convex surface of the β-sheet, forming key hydrophobic interactions with P652, H670, H677, and P681 (Fig. S6*A*). A W655S mutation was previously predicted to disrupt WW domain folding (9), and we confirmed this by ^{1}H-^{15}N heteronuclear single quantum coherence (HSQC) NMR spectroscopy. The wild-type [^{15}N]-labeled WW domain spectrum showed well-dispersed peaks consistent with an all-β structure. In contrast, WW^{W655S} yielded clustered peaks with a narrow dispersion between 7.5 and 8.5 ppm, characteristic of a protein without well-defined secondary structures (Fig. S6*B*). Additionally, the catalytic efficiency of USP8^{W655S} was increased eightfold ((146 ± 14) $\times 10^3$ M^{-1} s^{-1}) relative to wild-type (Fig. 2*B*), suggesting that a folded WW domain is a requisite for autoinhibition.

Our DUB activity assays showed that the WW domain increased K_M, implying decreased substrate affinity. We investigated this further by measuring the equilibrium dissociation constants (K_D) of wild-type USP8 and USP8$^{\Delta WW}$ for mono-Ub using fluorescence polarization (FP). The K_D values were determined to be 1.48 ± 0.37 μM and 0.29 ± 0.016 μM, respectively (Fig. 2*E*). Deletion of the WW domain led to a five-fold decrease in K_D, which agrees with the nine-fold decrease in apparent K_M observed in Ub-AMC kinetic assays (Table S2).

Next, the WW and WW^{W655S} domains were titrated against CD to measure inhibition in *trans*. To our surprise, this was not observed, even up to a 125,000-fold molar excess of the WW domain (Fig. S6*C*). We then decided to focus on

the WW:CD interaction in *cis* and the significance of the conserved linker between the domains (a.a. 686–757) (Fig. S7*A*). Constructs were designed by deleting the entire linker (Δ686–757), only the first half (Δ686–721), or only the second half (Δ722–757). The catalytic activity of USP8$^{\Delta 686-721}$ and USP8$^{\Delta 722-757}$ was unchanged compared to FL. However, deletion of the entire linker, as in USP8$^{\Delta 686-757}$, resulted in an eight-fold increase of catalytic efficiency (Fig. 2*B*). Using FP, the K_D of USP8$^{\Delta 686-757}$ for mono-Ub was determined to be 0.367 ± 0.019 μM, comparable to that measured for USP8$^{\Delta WW}$ (Fig. 2*E*).

As additional evidence to demonstrate autoinhibition in *cis*, we devised a strategy to reconstitute the WW-CD construct by sortase-mediated transpeptidation of the individual domains (26). Here, GB1-tagged WW or WW^{W655S} bearing a C-terminal LPETGG sortase recognition motif were ligated to CD$^{691-1110}$ bearing an N-terminal GGG motif. Ligation resulted in a relatively traceless WW-CD product analogous to the wild-type polypeptide (Fig. 2*F*). The time-course of DUB activity showed attenuation when CD was ligated with GB1-WW, but not with GB1-WW^{W655S} (Fig. 2*G*). Overall, these data suggest the linker between the WW domain and CD acts as a flexible tether mediating the spatial constraint and dynamics necessary for autoinhibition.

The WW domain inhibits USP8 activity by binding the S1 pocket

Inhibition by the WW domain in *trans* could not be detected using the Ub-AMC DUB assay. This suggests the WW:CD interaction may be weak and readily outcompeted by substrate Ub. Thus, we turned to NMR to directly characterize the interaction and circumvent enzyme activity as a readout. Upon the addition of a fivefold molar excess of unlabelled CD, a majority of the peaks in the ^{1}H-^{15}N HSQC spectrum of the [^{15}N]-WW domain were significantly attenuated (average $I/I_0 \leq 0.2$), indicating a direct interaction with the CD (Fig. 3, *A* and *B*). Fitting the intensities of select peaks suggested a K_D of ~20 μM (Fig. S8). The competition between the WW domain and Ub for the S1 pocket was confirmed by a titration of unlabeled Ub with segmentally labelled [^{15}N]WW-[^{14}N]CD (generated by sortase-mediated ligation). The addition of Ub resulted in significant increases in the intensities of [^{15}N]WW peaks, most likely due to the liberation of [^{15}N]WW from the S1 pocket (Fig. 3, *C* and *D*).

It was previously suggested that the WW domain forms a lid over the S1 Ub binding site by interacting with the CD at F1014 on blocking loop 1 (BL1) (9). However, F1014 resides in a hydrophobic cluster and interacts with the sidechains of L1063, Y1102, and H1059 (Fig. S9*A*). Mutation of F1014 to probe the interaction with the WW domain may disrupt CD structure and cause an extraneous change in enzyme activity independent of the WW domain interaction. To test this, we purified and measured the DUB activity of USP8^{F1014A} and USP8$^{\Delta WW.F1014A}$. Interestingly, both mutants exhibited product inhibition, a phenomenon not seen with any other construct used in this study (Fig. S9*B*). Compared to the wild-
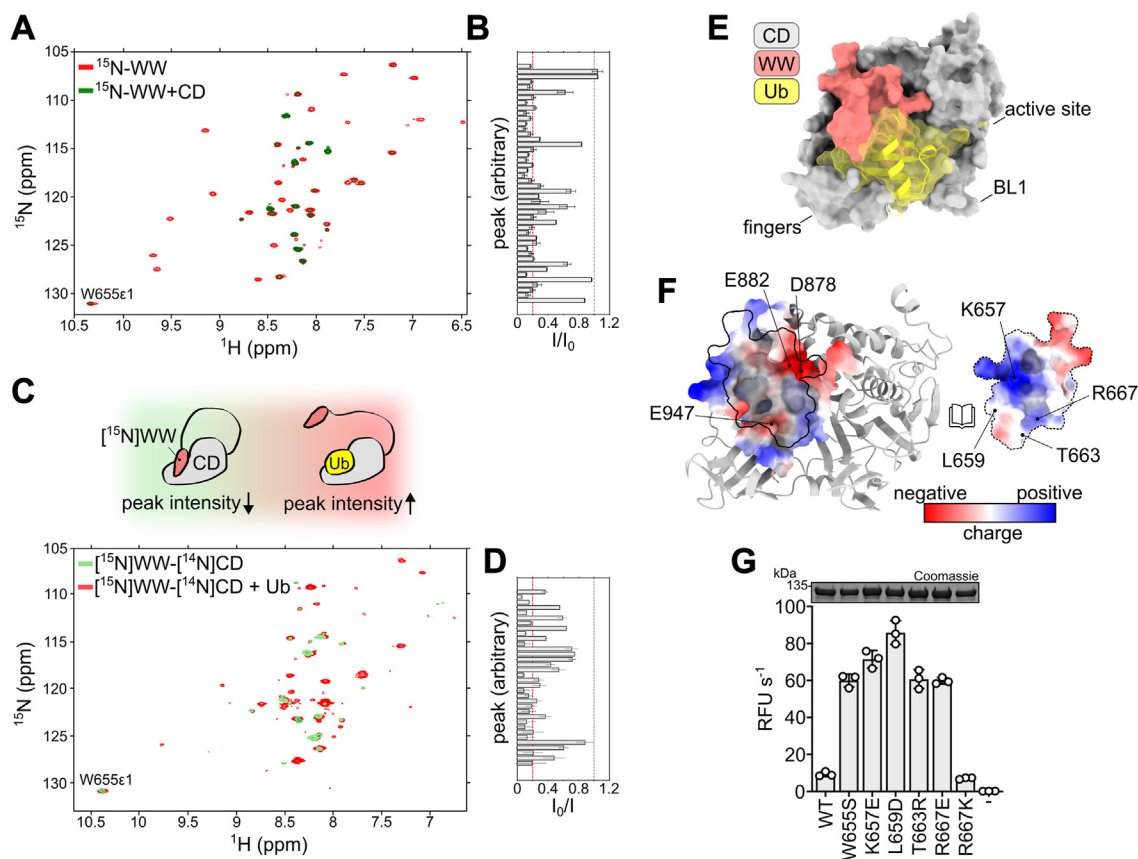
Figure 3. The WW domain competes with Ub by binding the S1 pocket. *A*, ^{1}H-^{15}N HSQC spectra of 40 μM [^{15}N]WW in the absence (*red*) or presence (*green*) of 202 μM unlabelled CD. Data were recorded at 14.1 T and 15 °C. *B*, changes in peak intensities in *A* were quantified as I/I_0, where I is the intensity of a resonance in the ^{1}H-^{15}N HSQC spectrum of [^{15}N]WW in the presence of CD, and I_0 is the corresponding intensity in the absence of CD. *C*, ^{1}H-^{15}N HSQC spectra of 50 μM segmentally-labelled [^{15}N]WW-[^{14}N]CD in the absence (*green*) or presence (*red*) of 300 μM unlabelled Ub. *D*, changes in peak intensities in *C* were quantified as I_0/I, where I_0 is the intensity of resonance in the ^{1}H-^{15}N HSQC spectrum of [^{15}N]WW-[^{14}N]CD in the absence of Ub, and I is the corresponding intensity in the presence of Ub. *E*, superposition of the USP8 CD (*grey*) bound to the WW domain (*salmon*) and Ub (*yellow*). Structures were predicted using AF2-Multimer. *F*, surface electrostatic potential representation of the WW:CD binding interface. Interacting residues are indicated. *G*, DUB activity of FL USP8 mutants (10 nM) was measured using 1 μM Ub-AMC (n = 3).

type, USP8^{F1014A} was significantly more active in terms of catalytic efficiency, with a relatively unchanged k_{cat} (0.16 ± 0.01 s^{-1}) but an eight-fold decrease in K_M (1.7 ± 0.3 μM) (Table S2). It is likely that mutation of F1014 disturbs the CD structure rather than the interaction with the WW domain.

We wanted to identify a more plausible inhibitory conformation for the WW domain. The AF2 model of USP8 has high PAE scores for interdomain residue pairs between the WW domain and CD. An optimized framework for predicting protein complex quaternary structures, known as AF2-Multimer, was recently described (27), and we implemented it in ColabFold (28) to improve the predicted structure of USP8. The result was a structure with distinct regions of low PAE scores corresponding to a high-confidence WW:CD interdomain interaction (Figs. S3 and S10A). To confirm this, we modeled the binary complex using the individual polypeptide sequences as input (WW+CD). We found that the conformation was nearly identical to that in the FL model (C_α r.m.sd ≈ 0.3 Å) (Fig. S10B) and thus, chose to focus analyses on WW+CD. Evaluation using DockQ (29) showed a pDockQ score of 0.332 and a positive predictive value (PPV) >0.83, suggesting a reasonably reliable prediction. In addition, the

AF2-Multimer prediction of the *Danio rerio* USP8 structure also revealed a similar WW:CD complex (Fig. S10C).

The modeled structure shows the WW domain inserted into the S1 pocket with the β1-β2 loop positioned at the base of the fingers subdomain. Compared to the orientation of bound Ub (predicted with AF2-Multimer; predicted local distance difference test, pLDDT >90, pDockQ 0.695, PPV >0.98), the WW domain was perched higher, making no contacts with the tips of the fingers, the BLs, or F1014 (Fig. 3E). The buried surface area at the WW:CD interface was 1151 Å^2, compared to 2093 Å^2 for Ub:CD.

Analysis of the WW:CD interface (Fig. S10D) revealed fundamental ionic interactions involving highly conserved CD residues (Figs. 3F, S7B, and S10E). CD^{D878} and CD^{E882} form salt bridges with the sidechain of WW^{K657}. Based on the predicted Ub-bound structure model, CD$^{D878/E882}$ also interact with Ub^{K48}. Furthermore, we observed a salt bridge between CD^{E947} and WW^{R667}, as well as an interaction between CD^{E947} and the backbone of Ub^{T66}. In addition, WW domain residues L659 and T663 on the β1-β2 loop are positioned in a hydrophobic patch deep in the S1 cleft. The importance of the aforementioned WW domain residues at the WW:CD

interface was assessed by mutagenesis in the context of FL USP8. Relative to the wild-type, all the mutants had increased activity with levels comparable to the uninhibited mutant USP8[W655S]. However, a conservative R667K mutation had no effect on DUB activity and USP8 remained autoinhibited. This suggests that the mutated interface residues are critical in mediating autoinhibition (Fig. 3*G*). Notably, except for W655S, the mutations to the WW domain did not significantly alter its conformation as the circular dichroism spectra of the isolated domains were indistinguishable from wild-type (Fig. S10*F*). Altogether, the mutagenesis data strongly supports the AF2-Multimer model.

AMP-activated protein kinase specifically phosphorylates purified USP8

The linker between the WW domain and CD harbors the 14-3-3BM, which contains the critical regulatory phosphosite pS718 and is a hotspot of somatic mutations in Cushing's disease patients (9, 14, 17, 30). As we sought to investigate how 14-3-3 binding impacts phosphorylated USP8 (p-USP8) activity and regulation, we first had to identify a kinase specific to S718. Inspection of the conserved 14-3-3BM sequence showed complete overlap with the consensus motif of AMP-activated protein kinase (AMPK) (31), and a recent review of the human Ser/Thr phosphoproteome ranked AMPK as the most likely kinase (32). We purified the recombinant AMPK heterotrimer (33) and performed *in vitro* kinase assays using USP8 as a substrate. Phosphorylation was monitored using a bio-orthogonal ATPγS analog described previously (34). Incubating FL USP8 with AMPK showed robust time and concentration-dependent phosphorylation reversible by lambda protein phosphatase (Fig. 4, *A* and *B*). Additionally, USP8[S718A] was not phosphorylated, suggesting the specificity of AMPK for S718. Mass spectrometry of AMPK-treated USP8 resolved the pS718-containing peptide (m/z 1904.816, $z = +1$) and no additional phosphosites (Fig. 4*C* and Table S3), further indicating the modification is stoichiometric and specific.

Phosphorylation and stimulation of AMPK using the upstream kinase CaMKKβ were used to show that the USP8 14-3-3BM may be an ideal substrate. Here, we compared the phosphorylation of the USP8 14-3-3BM as well as a SAMS 15-mer peptide (derived from rat acetyl-CoA carboxylase around S79) (35) by AMPK and p-AMPK. When the peptides were fused to the C-terminus of GST, only the wild-type 14-3-3BM and SAMS were phosphorylated, but not 14-3-3-BM[S718A] or GST alone (Fig. 4*D*). Surprisingly, both AMPK and p-AMPK phosphorylated the wild-type 14-3-3BM peptide equally well; however, the SAMS peptide was only phosphorylated by p-AMPK. These data show that AMPK is a potent *in vitro* kinase for USP8 with specificity for S718.

14-3-3 potentiates the inhibitory effect of the WW domain

Next, we wanted to analyze the impact of 14-3-3 binding on the WW-mediated inhibition of USP8. His-tagged FL USP8 or USP8[S718A], either treated with p-AMPK or not, was incubated with untagged 14-3-3γ. As expected, 14-3-3γ co-purified only

with the wild-type p-USP8 (Fig. S11). SEC-MALLS determined a p-USP8:14-3-3γ complex composed of one molecule of USP8 and one constitutive 14-3-3γ dimer. Compared to p-USP8 alone, the chromatographic peak was broad and eluted earlier (Fig. 5*A*).

We next measured the DUB activity of FL USP8 and USP8[ΔWW], treated with AMPK or not, as a titration with 14-3-3γ. Only p-USP8 was inhibited by incubation with 14-3-3γ, with an apparent relative IC$_{50}$ of 31.1 nM (Fig. 5*B*). Notably, even at high 14-3-3γ concentrations, USP8 maintained ∼25% of its activity, meaning 14-3-3γ binding attenuated but did not abolish DUB activity. As expected, non-phosphorylated USP8 and USP8[ΔWW] did not respond to 14-3-3γ, even up to 5 μM, a 1000-fold molar excess. Intriguingly, p-USP8[ΔWW] was also not inhibited by 14-3-3γ. These data indicate that 14-3-3 binding potentiates the autoinhibitory effect of the WW domain. We reason that this occurs due to a stabilized autoinhibited conformation, *i.e.* a WW:CD complex. Consistent with this, Michaelis-Menten kinetics of the p-USP8:14-3-3γ complex compared to non-phosphorylated USP8 in the presence of 14-3-3γ revealed a 2.4-fold increase of K_M (Figs. 5*C*, S4, and, Table S2). Compared to USP8[ΔWW], p-USP8:14-3-3γ has a 21.6-fold larger K_M (Table S2). The data show that the effect of 14-3-3 binding and WW-mediated inhibition primarily increases K_M, which is consistent with competitive inhibition.

Discussion

In this study, we characterized the autoinhibitory WW domain in USP8, revealing competitive binding to the S1 pocket. The WW:CD interaction was directly observed by NMR assays and a high-confidence complex structure was modeled using AF2-Multimer. Mutagenesis of WW domain residues at the predicted interaction interface abolished autoinhibition. Contrarily, molecular dynamics simulations presented by Kakihara and coauthors placed the WW domain over the S1 pocket like a lid, making contacts F1014 on BL1 in the CD (9). We could not reproduce these data here. Biochemical investigations on an F1014A mutation in the context of FL USP8 showed increased DUB activity. However, the Michaelis-Menten profile exhibited product inhibition, suggesting mutation of F1014 may significantly alter the CD structure, particularly in the region responsible for binding the Ub C-terminal tail. In support of a structural role for F1014, it is buried at the base of BL1 (15% solvent-accessible surface area), conserved, and hinders active site accessibility in some apo-USP structures, including USP8 (6, 10, 36–38). A similar occurrence of product inhibition was described for USP2, albeit for N221, an active site-adjacent residue (39).

Surprisingly, incubating the WW domain and CD in *trans* did not result in inhibition when using the Ub-AMC assay as a readout. Despite ^{1}H-^{15}N HSQC NMR confirming the formation of a complex, the WW:CD affinity was estimated to be about 20 μM, significantly lower than the 1.5 μM K_D of USP8 for Ub as determined by FP. Thus, when the WW domain is in *trans*, Ub readily outcompetes it for the S1 pocket. Only in *cis* does the WW domain substantially attenuate USP8 DUB
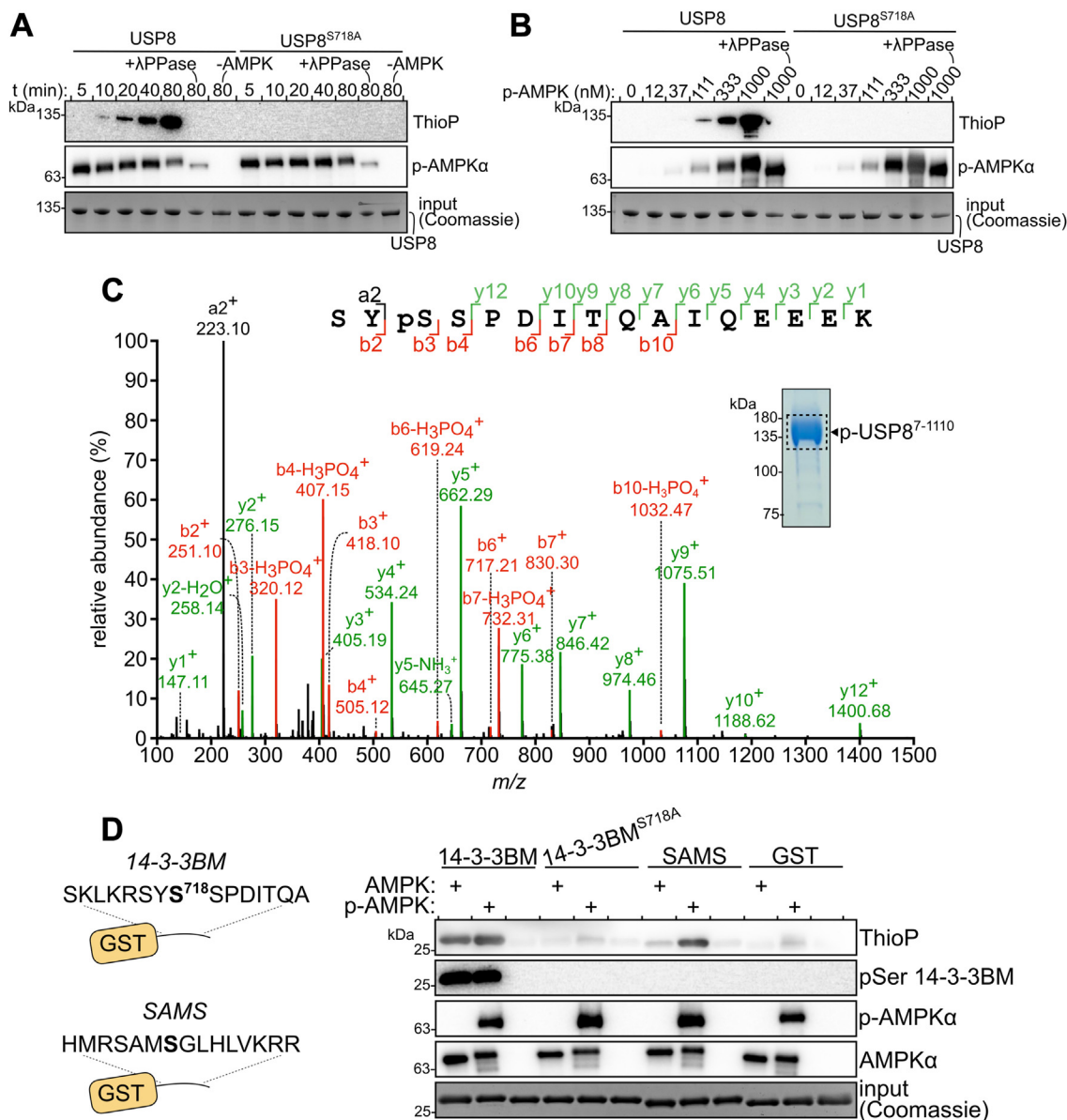
Figure 4. AMPK phosphorylates USP8 S718 *in vitro*. AMPK phosphorylates USP8 in a (*A*) time and (*B*) concentration-dependent manner. *C*, MS/MS spectrum of the pS718-containing peptide at *m/z* 1904.816 (*z* = +1). FL USP8 was incubated with p-AMPK and the sample was separated on a polyacrylamide gel before in-gel digest using trypsin/LysC and subsequent MS analysis. *D*, phosphorylation of GST-tagged 14-3-3BM wild-type, 14-3-3BM[S718A], SAMS, or GST alone using either AMPK or p-AMPK.

activity, highlighting the importance of proximity for potent autoinhibition.

Previous studies have shown that the 14-3-3BM is a multi-phosphorylated motif. Y717 is phosphorylated by the tyrosine receptor kinase EGFR ([40](#)), unknown kinases phosphorylate S718 at the cellular level, and multiple high-throughput phosphoproteomics studies showed that S716 and S719 could also be phosphorylated *in vivo*. However, the impact on the function of USP8 remains elusive. This raises an intriguing question about the order of phosphorylation of these sites, the responsible kinases, and their roles in regulating USP8. Using bioinformatical and biochemical analyses, we identified AMPK as a potent and specific *in vitro* kinase for S718. Attempts were made to demonstrate this *in vivo* using various methods,

including AMPK activation, pharmacological inhibition ([41](#)), overexpression, and knockdown, but the data (not shown) were inconclusive. The 14-3-3BM is a hotspot for regulation by phosphorylation, which complicates our efforts to interpret the cellular data of AMPK modulation. Validating that AMPK is the *in vivo* kinase for USP8 and delineating its role in the crosstalk with other kinases on the 14-3-3BM comprises a major task that goes beyond the scope of the current study. Despite this, determining AMPK as a highly specific kinase for S718 *in vitro* facilitated further investigations on phosphorylated USP8 and the interplay between 14-3-3 binding and activity regulation. The binding of 14-3-3γ to p-USP8 potentiated autoinhibition by the WW domain, whereas 14-3-3γ binding to a WW domain-deleted mutant of p-USP8 had no
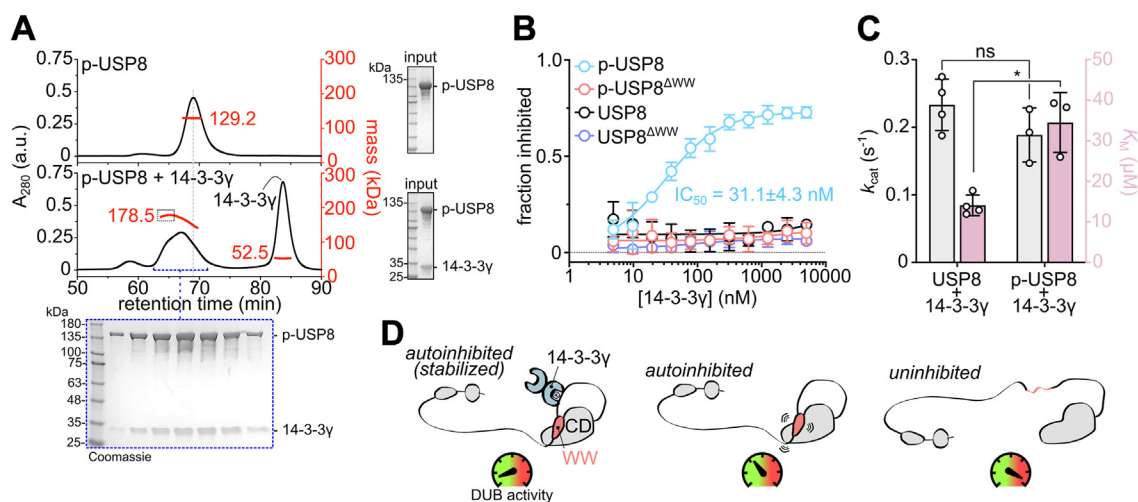
Figure 5. 14-3-3 potentiates the inhibitory effect of the WW domain. *A*, SEC-MALLS of 4 mg mL^{-1} pS718 USP8 (p-USP8) in isolation or incubated with 14-3-3γ (1:4 n:n). *B*, titration of 5 nM USP8 or USP8$^{\Delta WW}$, phosphorylated by AMPK or not, with 5 nM–5 μM 14-3-3γ. DUB activity was measured using 1 μM Ub-AMC (n = 3). *C*, Michaelis-Menten kinetics of 20 nM USP8 and p-USP8 in the presence of 10 μM 14-3-3γ, assayed using Ub-AMC. Kinetic parameters k_{cat} and K_M are presented. Data represent the mean and standard deviation of three or four independent experiments. Not significant, ns; *$p < 0.05$ (n = 3 or 4). *D*, representation of three distinct conformations of USP8 and the varying levels of DUB activity. When phosphorylated and bound by 14-3-3, USP8 is in a stabilized autoinhibited state and has the lowest activity levels (*left*). Non-phosphorylated UPS8 that is no longer bound by 14-3-3 remains downregulated by the WW domain, but the interaction is less stable, increasing activity (*middle*). Abolishing the WW:CD interaction renders USP8 dysregulated, resulting in a pathological hyperactive state (*right*).

effect. The K_M of the p-USP8:14-3-3γ complex, which is expected to account for a significant proportion of cellular USP8 (9), was more than two-fold greater than unbound USP8. As such, 14-3-3 stabilizes the autoinhibited conformation.

While it is known that somatic mutations in the 14-3-3BM drive Cushing's disease (17), mutations in the WW domain affecting its structure or ability to bind the CD may also be pathological. W655R and K657E/N mutations were identified in whole-exome sequencing of chronic lymphocytic leukemia (42), and R667C/H mutations have been detected in colorectal cancers (43). Our biochemical data and structure models suggest mutation of W655 unfolds the WW domain. In contrast, mutation of K657 or R667 disrupts the WW:CD complex as these residues participate in essential interactions at the interface.

Sequence analysis of vertebrate USP8 orthologs shows striking conservation of the WW domain and the linker connecting it to the CD. More distant invertebrate orthologs, such as *Drosophila melanogaster*, lack the WW domain entirely. We showed that deleting the WW domain in *Mus musculus* USP8 increased DUB activity and that modeling the structure of the *D. rerio* ortholog (53% sequence identity) generated a homologous structure with the WW domain predicted to occupy the S1 pocket. This suggests that WW-mediated regulation is an evolutionarily acquired mechanism of unknown origin. Interestingly, along with the 14-3-3BM, the WW-CD linker contains one of the three SH3 BMs that bind several scaffold proteins, including signal transducing adaptor molecule (STAM) (44). An intriguing possibility is that STAM binding, much like 14-3-3, modulates USP8 activity. Compounded with multiple phosphorylation sites in the linker region, this opens up the possibility of additional modes of regulation, such as other interacting proteins functioning as regulators *via* WW domain-dependent mechanisms.

Of the relatively few well-characterized USPs with known mechanisms of intramolecular regulation, all have exhibited autoactivation mediated by auxiliary domains (4, 6, 36, 45). This makes USP8 a unique case of intramolecular auto-inhibition, and whether other USPs also contain intrinsic inhibitory regions remains to be seen. Interestingly, the regulation of USP8 activity is surprisingly analogous to the regulation of USP7. The HUBL domain in USP7 potently activates the enzyme 100-fold in *cis*. Yet, in *trans*, the activation is significantly less, indicating that tethering the regulatory domain to the CD is critical for regulating some USPs. Furthermore, a binding partner, GMP synthase, potentiates the stimulatory effect of the HUBL domain by stabilizing the autoactivated conformation in USP7 (4, 36). In the case of USP8, the WW domain in *cis* is potently autoinhibiting, and 14-3-3 proteins potentiate this by binding phosphorylated USP8 and stabilizing the autoinhibited conformation. Interestingly, WW domain-mediated regulation of catalytic activity has been observed in the HECT E3 Ub ligase Smurf2 (46) and the proline peptidyl isomerase Pin1 (47), thus highlighting WW domains as regulators of enzymatic activity.

Overall, the data allow for the interpretation of three distinct conformations of USP8 with varying levels of activity (Fig. 5D). The first is a stabilized autoinhibited state with the lowest activity in which USP8 is phosphorylated at S718 and bound by 14-3-3. The second conformation, still autoinhibited, is non-phosphorylated, and the WW:CD interaction is weakened due to the loss of 14-3-3 binding. USP8 is slightly more active in this state but within the presumed physiological range. Lastly, the third conformation is completely uninhibited due to the loss of the WW:CD interaction, either because of mutations to interacting residues at the interface or mutations disrupting the WW domain structure. In this conformation,

USP8 is hyperactive and may represent the pathological proteoform.

Experimental procedures

Expression and purification of USP8

FL USP8 constructs (a.a. 7–1110), including ΔWW, Δlinker, and point mutants, were expressed from pNIC-CH vectors bearing a C-terminal His$_6$ tag (Table S4). Saturated starter cultures were diluted 100-fold and grown at 37 °C with shaking until an OD$_{600}$ of 1.5 was reached. The incubator temperature was then reduced to 18 °C, and cultures were left shaking for 1 h. Protein expression was induced by the addition of 0.2 mM isopropyl-β-D-thiogalactopyranoside and incubated for 20 h. Cells were harvested, and pellets flash frozen before being resuspended in Buffer R (50 mM tris pH 8.0, 0.5 M NaCl, 5% glycerol, 1 mM MgCl$_2$, 5 mM imidazole) supplemented with 3 mM β-mercaptoethanol (BME), 0.5 mM phenylmethylsulfonyl fluoride, benzonase (*S. marcescens*), and lysozyme. Cells were lysed by sonication (60% amplitude, 5 min per sample using pulses of 10/30 s on/off, Qsonica 500) and the insoluble material was removed by centrifugation. Equilibrated Ni^{2+}-nitriloacetic acid-conjugated agarose was added to the supernatant and incubated on a rotary incubator at 4 °C for 60 min before being poured into a gravity-fed column. The resin was washed with 30 column volumes of Buffer R containing 15 mM imidazole. Bound proteins were eluted with Buffer R containing 400 mM imidazole. Using an AKTA Pure FPLC (Cytiva), the eluate was loaded onto a HiLoad 16/600 Superdex 200 pg column equilibrated with Buffer S (25 mM tris pH 8.5, 0.15 mM NaCl, 2 mM BME) at a flow rate of 1 ml min^{-1}. Fractions containing USP8 were pooled and further purified by high-resolution anion exchange using a 5/50 Gl Mono Q column (Cytiva) at 1 ml min^{-1}. The sample was loaded using binding buffer (Buffer A: 25 mM tris pH 8.5) and eluted using a 20 CV linear gradient of elution buffer (Buffer B: 25 mM tris pH 8.5, 1 M NaCl). The typical yield of pure FL USP8 was 0.2 to 0.5 mg per litre of culture.

Before aliquoting and flash freezing, the purity of all protein preparations was determined by SDS-PAGE, and the concentrations were measured using OD$_{280}$ and the estimated molar extinction coefficients derived from the amino acid sequences (Expasy ProtParam).

SEC-SAXS

SAXS was performed at BioCAT (beamline 18ID at the Advanced Photon Source, Chicago) with in-line SEC. A 350 μl sample of 2 mg mL^{-1} FL USP8 was injected onto a 10/300 Gl Superdex 200 Increase column (Cytiva) at a flow rate of 0.6 ml min^{-1} using an AKTA Pure FPLC (Cytiva). After passing through a UV monitor, the eluate was flown through the SAXS co-flow cell to reduce radiation damage (48). Scattering intensity was recorded using an Eiger2 XE 9M (Dectris) detector 3.6 m away, giving access to a q-range of 0.003 to 0.42 Å^{-1}. Exposures were acquired for 0.5 s every 1 s during elution, and the data were reduced using BioXTAS RAW 2.1.3. Buffer blanks were created by subtracting the average scattering intensity of a region flanking the elution peak. The resulting $I(q)$ *versus* q curves were used for subsequent analyses. Low-resolution *ab initio* shape envelopes were determined using the program DAMMIN from the ATSAS package. Twenty independent reconstructions were performed and superimposed using SUPCOMB and averaged by DAM-AVER using normalized spatial discrepancy criteria. Refinement *via* DAMSTART and DAMMIN was used to generate the final model.

SEC-MALLS

The absolute molar masses and mass distributions of purified USP8, p-USP8, and the p-USP8:14-3-3γ complex were determined using SEC-MALLS. USP8 was analyzed at 2, 4, and 8 mg mL^{-1}, and p-USP8 was analyzed at 4 mg mL^{-1}. The complex sample was prepared by incubating p-USP8 and 14-3-3γ at a 1:4 ratio (n:n) on ice for 2 h. Samples were loaded onto a 10/300 Gl Superose 6 column (Cytiva) equilibrated in 25 mM tris pH 7.2, 0.15 M NaCl and 1 mM tris(2-carboxyethyl)phosphine followed by an in-line MiniDAWN TREOS and Optilab T-rEX (Wyatt Technologies). Samples were run at ambient temperature at 0.2 ml min^{-1}. Mass calculations were performed using ASTRA 6.1.1.17 (Wyatt Technologies), assuming a refractive index increment (dn/dC) of 0.185 ml g^{-1}.

Ub-AMC DUB assays

Ub-AMC cleavage assays were performed in USP8 kinetic buffer (20 mM tris pH 7.2, 0.1 M NaCl, 2 mM dithiothreitol) at 25 °C in black 384-well flat bottom plates (non-binding surface, Corning) in a final volume of 20 μl. Purified USP8 constructs (1.5–40 nM) were mixed 1:1 with varying concentrations of Ub-AMC (Bio-Techne) ranging from 39 nM–40 μM, which were prepared as a two-fold dilution series. Fluorescence (λ_{ex} 345 nm, λ_{em} 445 nm) was measured at 30 s intervals for 5 min using a Cytation 5 multimode plate reader (Agilent). For the Michaelis-Menten analysis, the initial rates were plotted as a function of Ub-AMC concentration and fitted with the equation:

$$V = (V_{max} \times [S]) / ([S] + K_M)$$

using Prism 10.0.1 (GraphPad Software Inc). For instances of product inhibition, the model used to fit the data was instead:

$$V = (V_{max} \times [S]) \left/ \left([S] \left(1 + \frac{[S]}{K_i} \right) + K_M \right) \right.$$

where K_i is the dissociation constant for the bound, inhibitive product. The means and standard deviations were extracted from three or four replicates. For the inhibition of USP8 by the WW-like domain in *trans*, 2 nM USP8 was incubated with 0.39 nM–400 μM WW-like domain at ambient temperature for 30 min before adding 2 μM Ub-AMC. Similarly, assays examining the inhibition of USP8 by 14-3-3γ were performed using 5 nM USP8 and 5 nM–

5 μM 14-3-3γ. The mean and standard deviation were extracted from four replicates. The steady-state kinetic analysis of the USP8:14-3-3γ complex was performed by incubating 20 nM USP8 with 10 μM 14-3-3γ for 15 min at ambient temperature before the addition of 19.5 nM–20 μM Ub-AMC. The mean and standard deviation were extracted from four replicates.

Sortase-mediated transpeptidation (sortagging)

The USP8 WW domain and CD were ligated using an engineered sortase A variant from *S. aureus* (eSrtA) (26) under the conditions previously described (49). An LPETGG recognition motif was cloned onto the C-terminus of His_8-GB1-WW constructs. The acceptor domain, USP8 $CD^{691-1110}$, was designed with an N-terminal GGG motif exposed following the cleavage of a His_8-GB1 tag using TEV. The optimal ligation reaction was performed for 15 to 30 min at ambient temperature in Buffer SML (50 mM tris pH 7.5, 0.1 M NaCl, 5 mM $MgCl_2$, 0.5 mM TCEP). A 10:1 ratio (n:n) of N-terminal domain to C-terminal acceptor was used by incubating 200 μM WW^{LPETGG} and 20 μM ^{GGG}CD in the presence of 5 μM eSrtA. To yield a segmentally labelled WW-CD construct for ^1H-^{15}N HSQC, ^{15}N isotopically labelled GB1-WW^{LPETGG} was ligated onto unlabelled ^{GGG}CD. The N-terminal GB1 tag was removed simultaneously by incubation with TEV, and the resulting $WW^{LPETGGG}CD$ product was isolated using analytical gel filtration on a 10/300 Gl Superdex 200 increase column equilibrated with Buffer NMR (20 mM sodium phosphate pH 6.5, 0.1 M NaCl) at 0.4 ml min^{-1}.

NMR experiments

All NMR experiments were performed on a 600 MHz Bruker Avance III NMR spectrometer equipped with a 5 mm TCI cryoprobe. All ^1H-^{15}N HSQC spectra were acquired with a 1.5 s interscan delay and acquisition times of 41 ms and 64 ms, as well as 70 and 640 complex points in the t_1 and t_2 dimensions, respectively. Carriers were positioned in the center of the water resonance (∼4.673 ppm) and 119 ppm for ^1H and ^{15}N, respectively. Spectra were processed using NMRPipe (50) and visualized using NMRFAM-SPARKY (51).

Proteins were exchanged into buffer NMR containing 7% D_2O before NMR data acquisition. To obtain the binding affinity between WW and CD in *trans*, a titration was carried out in which unlabeled CD was added to [^{15}N]-labeled WW (maintained at 100 μM) in a series of seven steps at a total concentration of 0, 30, 60, 95, 160, 240, and 335 μM. Given the molecular weight of the WW-CD complex (53.85 kDa), we anticipate that the majority of the resonances in the structured region of the WW domain would broaden beyond detection in the CD-bound state. We used a one-site binding model (P + L $\rightleftharpoons$ PL) to extract the K_D value. Curve fitting assumed that peak intensities of the resonances in the structured region of the WW domain were

proportional to the fractional population of the free WW domain, described by the following equation:

$$I = I_{\text{free}} \bullet p_{\text{free}} =$$

$$I_{\text{free}}\left(1 - \frac{P_T + L_T + K_d - \sqrt{(P_T + L_T + K_D)^2 - 4P_T L_T}}{2P_T}\right)$$

where I_{free} is the peak intensity of the free WW domain, p_{free} is the fractional population of the free WW domain, P_T and L_T are the total concentrations of WW and CD, respectively, and K_D is the dissociation constant. The assumption is valid in two scenarios: (i) resonances are in the extremely slow chemical exchange regime ($k_{\text{ex}} \ll \Delta\omega$), (ii) resonances do not have chemical shift perturbations (*i.e.* located distant from the binding interface) and $k_{\text{ex}} \ll R_{2,\text{bound}} - R_{2,\text{free}}$. A subset of resonances is fitted with this model using an in-house Python script. Uncertainty of the K_D values was obtained from the covariance matrix.

AlphaFold2-Multimer structure modelling with ColabFold

Query sequences for human USP8 (uniprot p40818) FL (a.a. 1–1118), $USP8^{WW\text{-}CD}$ (a.a. 645–1118), $USP8^{WW}$ (a.a. 645–685), $USP8^{CD}$ (a.a. 686–1118), *D. rerio* USP8 (uniprot a0a8mp169), and Ub (a.a. 1–76) were input into ColabFold v1.5.3 accessing NVIDIA V100 GPUs. AlphaFold2-Multimer v3 was used for structure modelling, mainly running default settings. Sequence alignments were generated with MMseqs2 and HHsearch, and predictions were obtained from a combination of paired and unpaired multiple sequence alignments. The top-ranked structure was relaxed with AMBER. Coot (52) (v0.9.8.92) was used to reduce the number of Ramachandran outliers and clashes. Model accuracy was assessed by pLDDT (>85), PAE (<15 Å), and predicted DockQ scores (pDockQ ≥ 0.23) (29, 53).

In vitro kinase assays

All kinase reactions were performed at ambient temperature in Buffer KABI (Abcam: 5 mM MOPS pH 7.2, 2.5 mM β-glycerol-phosphate, 5 mM $MgCl_2$, 1 mM EGTA, 0.4 mM EDTA, and 1 mM DTT) supplemented with 0.25 mM ATP and 0.25 mM AMP. For thiophosphorylation experiments, 0.25 mM ATPγS (Bio-Techne) was used instead of ATP. Unless otherwise stated, the substrate:AMPK ratio was maintained at 25:1 (n:n) and p-AMPK was used. Before immunoblotting, thiophosphorylated proteins were alkylated with *p*-nitrobenzyl mesylate (PNBM) (Abcam) per the manufacturer's instructions. Briefly, kinase reactions were quenched by mixing 1:1 with 20 mM EDTA, then 2.5 mM PNBM was added, and the mixture was incubated for 2 h at ambient temperature. The resulting thiophosphate ester moiety was detected by immunoblot using the thioP antibody (34). For the detection of pS718 in the USP8 14-3-3BM, an anti-pS-14-3-3BM primary antibody was also used. In this case, the thiophosphorylated samples were not

treated with PNBM. Dephosphorylation was achieved by incubating 25 µg of phosphorylated protein with 400 U of lambda phage dual specificity phosphatase (NEB) at 30 °C for 30 min.

For additional methods, refer to Supporting Information, Extended Methods.

Data availability

All processed data are available in the article and supporting information. SAXS data have been deposited to the Small Angle Scattering Biological Data Bank (54) (accession SASDU39).

Author contributions—L. F., R. J. H., P. O. V., Y. T., Z. Z., and R. H. formal analysis; L. F., J. M., A. A. D., Y. L., R. J. H., P. O. V., M. B., C. C., and R. H. investigation; Y.-X. W., Y. T., Z. Z., and R. H. supervision; M. B. visualization; C. C. and Y. T. writing–review & editing; C. C. writing–original draft; C. C. and Y. T. validation; C. C. methodology; C. C. and Y. T. conceptualization. Y. T. resources.

Conflict of interest—The authors declare that they have no conflicts of interest with the contents of this article.

Abbreviations—The abbreviations used are: a.a., amino acid; AF, AlphaFold; AMC, 7-amino-4-methylcoumarin; DUB, deubiquitinase; FL, full-length; FP, fluorescence polarization; HSQC, heteronuclear single quantum coherence; PAE, predicted aligned error; pLDDT, predicted local distance difference test; SAXS, small-angle X-ray scattering.

References

1. Yau, R., and Rape, M. (2016) The increasing complexity of the ubiquitin code. *Nat. Cell Biol.* **18**, 579–586
2. Komander, D., and Rape, M. (2012) The ubiquitin code. *Annu. Rev. Biochem.* **81**, 203–229
3. Komander, D., Clague, M. J., and Urbé, S. (2009) Breaking the chains: structure and function of the deubiquitinases. *Nat. Rev. Mol. Cell Biol.* **10**, 550–563
4. Faesen, A. C., Luna-Vargas, M. P. A., Geurink, P. P., Clerici, M., Merkx, R., van Dijk, W. J., *et al.* (2011) The differential modulation of USP activity by internal regulatory domains, interactors and eight ubiquitin chain types. *Chem. Biol.* **18**, 1550–1561
5. Kim, R. Q., van Dijk, W. J., and Sixma, T. K. (2016) Structure of USP7 catalytic domain and three Ubl-domains reveals a connector α-helix with regulatory role. *J. Struct. Biol.* **195**, 11–18
6. Clerici, M., Luna-Vargas, M. P. A., Faesen, A. C., and Sixma, T. K. (2014) The DUSP–Ubl domain of USP4 enhances its catalytic efficiency by promoting ubiquitin exchange. *Nat. Commun.* **5**, 5399
7. Gersch, M., Wagstaff, J. L., Toms, A. V., Graves, B., Freund, S. M. V., and Komander, D. (2019) Distinct USP25 and USP28 oligomerization states regulate deubiquitinating activity. *Mol. Cell* **74**, 436–451.e7
8. Sauer, F., Klemm, T., Kollampally, R. B., Tessmer, I., Nair, R. K., Popov, N., and Kisker, C. (2019) Differential oligomerization of the deubiquitinases USP25 and USP28 regulates their activities. *Mol. Cell* **74**, 421–435.e10
9. Kakihara, K., Asamizu, K., Moritsugu, K., Kubo, M., Kitaguchi, T., Endo, A., *et al.* (2021) Molecular basis of ubiquitin-specific protease 8 autoinhibition by the WW-like domain. *Commun. Biol.* **4**, 1272
10. Avvakumov, G. V., Walker, J. R., Xue, S., Finerty, P. J., Mackenzie, F., Newman, E. M., and Dhe-Paganon, S. (2006) Amino-terminal dimerization, NRDP1-rhodanese interaction, and inhibited catalytic domain conformation of the ubiquitin-specific protease 8 (USP8). *J. Biol. Chem.* **281**, 38061–38070
11. Ernst, A., Avvakumov, G., Tong, J., Fan, Y., Zhao, Y., Alberts, P., *et al.* (2013) A strategy for modulation of enzymes in the ubiquitin system. *Science* **339**, 590–595
12. Row, P. E., Liu, H., Hayes, S., Welchman, R., Charalabous, P., Hofmann, K., *et al.* (2007) The MIT domain of UBPY constitutes a CHMP binding and endosomal localization signal required for efficient epidermal growth factor receptor degradation. *J. Biol. Chem.* **282**, 30929–30937
13. Wu, X., Yen, L., Irwin, L., Sweeney, C., and Carraway, K. L. (2004) Stabilization of the E3 ubiquitin ligase Nrdp1 by the deubiquitinating enzyme USP8. *Mol. Cell Biol.* **24**, 7748–7757
14. Berlin, I., Schwartz, H., and Nash, P. D. (2010) Regulation of epidermal growth factor receptor ubiquitination and trafficking by the USP8·STAM complex. *J. Biol. Chem.* **285**, 34909–34921
15. Meyers, R. M., Bryan, J. G., McFarland, J. M., Weir, B. A., Sizemore, A. E., Xu, H., *et al.* (2017) Computational correction of copy number effect improves specificity of CRISPR–Cas9 essentiality screens in cancer cells. *Nat. Genet.* **49**, 1779–1784
16. Perez-Rivas, L. G., Theodoropoulou, M., Ferraù, F., Nusser, C., Kawaguchi, K., Stratakis, C. A., *et al.* (2015) The gene of the ubiquitin-specific protease 8 is frequently mutated in adenomas causing Cushing's disease. *J. Clin. Endocrinol. Metab.* **100**, E997–E1004
17. Reincke, M., Sbiera, S., Hayakawa, A., Theodoropoulou, M., Osswald, A., Beuschlein, F., *et al.* (2015) Mutations in the deubiquitinase gene USP8 cause Cushing's disease. *Nat. Genet.* **47**, 31–38
18. Jacques, D. A., and Trewhella, J. (2010) Small-angle scattering for structural biology—expanding the frontier while avoiding the pitfalls. *Protein Sci.* **19**, 642–657
19. Kikhney, A. G., and Svergun, D. I. (2015) A practical guide to small angle X-ray scattering (SAXS) of flexible and intrinsically disordered proteins. *FEBS Lett.* **589**, 2570–2577
20. Tesei, G., Trolle, A. I., Jonsson, N., Betz, J., Knudsen, F. E., Pesce, F., *et al.* (2024) Conformational ensembles of the human intrinsically disordered proteome. *Nature* **626**, 897–904
21. Schneidman-Duhovny, D., Hammel, M., Tainer, J. A., and Sali, A. (2016) FoXS, FoXSDock and MultiFoXS: single-state and multi-state structural modeling of proteins and their complexes based on SAXS profiles. *Nucleic Acids Res.* **44**, W424–W429
22. van Tol, B. D. M., van Doodewaerd, B. R., Lageveen-Kammeijer, G. S. M., Jansen, B. C., Talavera Ormeño, C. M. P., Hekking, P. J. M., *et al.* (2023) Neutron-encoded diubiquitins to profile linkage selectivity of deubiquitinating enzymes. *Nat. Commun.* **14**, 1661

23. Dong, K. C., Helgason, E., Yu, C., Phu, L., Arnott, D. P., Bosanac, I., *et al*. (2011) Preparation of distinct ubiquitin chain reagents of high purity and yield. *Structure* **19**, 1053–1063

24. Sudol, M., Chen, H. I., Bougeret, C., Einbond, A., and Bork, P. (1995) Characterization of a novel protein-binding module — the WW domain. *FEBS Lett.* **369**, 67–71

25. Macias, M. J., Hyvönen, M., Baraldi, E., Schultz, J., Sudol, M., Saraste, M., and Oschkinat, H. (1996) Structure of the WW domain of a kinase-associated protein complexed with a proline-rich peptide. *Nature* **382**, 646–649

26. Chen, I., Dorr, B. M., and Liu, D. R. (2011) A general strategy for the evolution of bond-forming enzymes using yeast display. *Proc. Natl. Acad. Sci. U. S. A.* **108**, 11399–11404

27. [Preprint] Evans, R., Neill, M. O., Pritzel, A., Antropova, N., Senior, A., Green, T., *et al*. (2022) Protein complex prediction with AlphaFold-Multimer. *bioRxiv*. https://doi.org/10.1101/2021.10.04.463034v2

28. Mirdita, M., Schütze, K., Moriwaki, Y., Heo, L., Ovchinnikov, S., and Steinegger, M. (2022) ColabFold: making protein folding accessible to all. *Nat. Methods* **19**, 679–682

29. Basu, S., and Wallner, B. (2016) DockQ: a quality measure for protein-protein docking models. *PLoS One* **11**, e0161879

30. Mizuno, E., Kitamura, N., and Komada, M. (2007) 14-3-3-dependent inhibition of the deubiquitinating activity of UBPY and its cancellation in the M phase. *Exp. Cell Res.* **313**, 3624–3634

31. Hardie, D. G., Schaffer, B. E., and Brunet, A. (2016) AMPK: an energy-sensing pathway with multiple inputs and outputs. *Trends Cell Biol.* **26**, 190–201

32. Johnson, J. L., Yaron, T. M., Huntsman, E. M., Kerelsky, A., Song, J., Regev, A., *et al*. (2023) An atlas of substrate specificities for the human serine/threonine kinome. *Nature*. https://doi.org/10.1038/s41586-022-05575-3

33. Li, X., Wang, L., Zhou, X. E., Ke, J., de Waal, P. W., Gu, X., *et al*. (2015) Structural basis of AMPK regulation by adenine nucleotides and glycogen. *Cell Res.* **25**, 50–66

34. Allen, J. J., Li, M., Brinkworth, C. S., Paulson, J. L., Wang, D., Hübner, A., *et al*. (2007) A semisynthetic epitope for kinase substrates. *Nat. Methods* **4**, 511–516

35. Davies, S. P., Carling, D., and Hardie, D. G. (1989) Tissue distribution of the AMP-activated protein kinase, and lack of activation by cyclic-AMP-dependent protein kinase, studied using a specific and sensitive peptide assay. *Eur. J. Biochem.* **186**, 123–128

36. Faesen, A. C., Dirac, A. M. G., Shanmugham, A., Ovaa, H., Perrakis, A., and Sixma, T. K. (2011) Mechanism of USP7/HAUSP activation by its C-Terminal ubiquitin-like domain and allosteric regulation by GMP-synthetase. *Mol. Cell* **44**, 147–159

37. Hu, M., Li, P., Li, M., Li, W., Yao, T., Wu, J. W., *et al*. (2002) Crystal structure of a UBP-family deubiquitinating enzyme in isolation and in complex with ubiquitin aldehyde. *Cell* **111**, 1041–1054

38. Molland, K., Zhou, Q., and Mesecar, A. D. (2014) A 2.2 Å resolution structure of the USP7 catalytic domain in a new space group elaborates upon structural rearrangements resulting from ubiquitin binding. *Acta Cryst. F* **70**, 283–287

39. Renatus, M., Parrado, S. G., D'Arcy, A., Eidhoff, U., Gerhartz, B., Hassiepen, U., *et al*. (2006) Structural basis of ubiquitin recognition by the deubiquitinating protease USP2. *Structure* **14**, 1293–1302

40. Kasahara, K., Aoki, H., Kiyono, T., Wang, S., Kagiwada, H., Yuge, M., *et al*. (2018) EGF receptor kinase suppresses ciliogenesis through activation of USP8 deubiquitinase. *Nat. Commun.* **9**, 758

41. Lemos, C., Schulze, V. K., Baumgart, S. J., Nevedomskaya, E., Heinrich, T., Lefranc, J., *et al*. (2021) The potent AMPK inhibitor BAY-3827 shows strong efficacy in androgen-dependent prostate cancer models. *Cell Oncol.* **44**, 581–594

42. Landau, D. A., Tausch, E., Taylor-Weiner, A. N., Stewart, C., Reiter, J. G., Bahlo, J., *et al*. (2015) Mutations driving CLL and their evolution in progression and relapse. *Nature* **526**, 525–530

43. Giannakis, M., Mu, X., Shukla, S., Qian, Z., Cohen, O., Nishihara, R., *et al*. (2016) Genomic correlates of immune-cell infiltrates in colorectal carcinoma. *Cell Rep.* **15**, 857–865

44. Kaneko, T., Kumasaka, T., Ganbe, T., Sato, T., Miyazawa, K., Kitamura, N., and Tanaka, N. (2003) Structural insight into modest binding of a non-PXXP ligand to the signal transducing adaptor molecule-2 Src homology 3 domain. *J. Biol. Chem.* **278**, 48162–48168

45. Avvakumov, G. V., Walker, J. R., Xue, S., Allali-Hassani, A., Asinas, A., Nair, U. B., *et al*. (2012) Two ZnF-UBP domains in isopeptidase T (USP5). *Biochemistry* **51**, 1188–1198

46. Ruetalo, N., Anders, S., Stollmaier, C., Jäckl, M., Schütz-Stoffregen, M. C., Stefan, N., *et al*. (2019) The WW1 domain enhances autoinhibition in Smurf ubiquitin ligases. *J. Mol. Biol.* **431**, 4834–4847

47. Strotz, D., Orts, J., Kadavath, H., Friedmann, M., Ghosh, D., Olsson, S., *et al*. (2020) Protein allostery at atomic resolution. *Angew. Chem. Int. Ed.* **59**, 22132–22139

48. Kirby, N., Cowieson, N., Hawley, A. M., Mudie, S. T., McGillivray, D. J., Kusel, M., *et al*. (2016) Improved radiation dose efficiency in solution SAXS using a sheath flow sample environment. *Acta Crystallogr. D Struct. Biol.* **72**, 1254–1266

49. Li, J., Zhang, Y., Soubias, O., Khago, D., Chao, F. A., Li, Y., *et al*. (2020) Optimization of sortase A ligation for flexible engineering of complex protein systems. *J. Biol. Chem.* **295**, 2664–2675

50. Delaglio, F., Grzesiek, S., Vuister, G. W., Zhu, G., Pfeifer, J., and Bax, A. (1995) NMRPipe: a multidimensional spectral processing system based on UNIX pipes. *J. Biomol. NMR* **6**, 277–293

51. Lee, W., Tonelli, M., and Markley, J. L. (2015) NMRFAM-SPARKY: enhanced software for biomolecular NMR spectroscopy. *Bioinformatics* **31**, 1325–1327

52. Emsley, P., Lohkamp, B., Scott, W. G., and Cowtan, K. (2010) Features and development of coot. *Acta Crystallogr. Sect. D: Biol. Crystallogr.* **66**, 486–501

53. Bryant, P., Pozzati, G., and Elofsson, A. (2022) Improved prediction of protein-protein interactions using AlphaFold2. *Nat. Commun.* **13**, 1265

54. Kikhney, A. G., Borges, C. R., Molodenskiy, D. S., Jeffries, C. M., and Svergun, D. I. (2020) SASBDB: towards an automatically curated and validated repository for biological scattering data. *Protein Sci.* **29**, 66–75

55. Azatian, S. B., Kaur, N., and Latham, M. P. (2019) Increasing the buffering capacity of minimal media leads to higher protein yield. *J. Biomol. NMR* **73**, 11–17

56. Robert, X., and Gouet, P. (2014) Deciphering key features in protein structures with the new ENDscript server. *Nucleic Acids Res.* **42**, W320–W324

57. Shevchenko, A., Tomas, H., Havliš, J., Olsen, J. V., and Mann, M. (2007) In-gel digestion for mass spectrometric characterization of proteins and proteomes. *Nat. Protoc.* **1**, 2856–2860

58. Svergun, D. I. (1992) Determination of the regularization parameter in indirect-transform methods using perceptual criteria. *J. Appl. Crystallogr.* **25**, 495–503

59. Di Tommaso, P., Moretti, S., Xenarios, I., Orobitg, M., Montanyola, A., Chang, J. M., *et al*. (2011) T-Coffee: a web server for the multiple sequence alignment of protein and RNA sequences using structural information and homology extension. *Nucleic Acids Res.* **39**, W13–W17

60. Franke, D., Jeffries, C. M., and Svergun, D. I. (2015) Correlation Map, a goodness-of-fit test for one-dimensional X-ray scattering spectra. *Nat. Methods* **12**, 419–422

61. Hopkins, J. B., Gillilan, R. E., and Skou, S. (2017) BioXTAS RAW: improvements to a free open-source program for small-angle X-ray scattering data reduction and analysis. *J. Appl. Crystallogr.* **50**, 1545–1553

62. Piiadov, V., Ares de Araújo, E., Oliveira Neto, M., Craievich, A. F., and Polikarpov, I. (2019) SAXSMoW 2.0: online calculator of the molecular weight of proteins in dilute solution from experimental SAXS data measured on a relative scale. *Protein Sci.* **28**, 454–463

63. Rambo, R. P., and Tainer, J. A. (2013) Accurate assessment of mass, models and resolution by small-angle scattering. *Nature* **496**, 477–481

64. Kozin, M. B., and Svergun, D. I. (2001) Automated matching of high- and low-resolution structural models. *J. Appl. Cryst.* **34**, 33–41

65. Goddard, T. D., Huang, C. C., Meng, E. C., Pettersen, E. F., Couch, G. S., Morris, J. H., and Ferrin, T. E. (2018) UCSF ChimeraX: meeting modern challenges in visualization and analysis. *Protein Sci.* **27**, 14–25

66. Pettersen, E. F., Goddard, T. D., Huang, C. C., Meng, E. C., Couch, G. S., Croll, T. I., *et al*. (2021) UCSF ChimeraX: structure visualization for researchers, educators, and developers. *Protein Sci.* **30**, 70–82

67. Tuukkanen, A. T., Kleywegt, G. J., and Svergun, D. I. (2016) Resolution of ab initio shapes determined from small-angle scattering. *IUCrJ* **3**, 440–447